Detection efficiency of a high-pressure gas scintillation proportional chamber

Frederic H. Fahey
Division of Nuclear Medicine, Department of Radiology, Georgetown University Hospital, Washington, DC 20007

Robert E. Zimmerman and Philip F. Judy
Department of Radiology, Harvard Medical School, Boston, Massachusetts 02115

Richard C. Lanza
Laboratory of Nuclear Science, Massachusetts Institute of Technology, Cambridge, Massachusetts 02141

(Received 23 April 1986; accepted for publication 14 October 1986)

The detection efficiency of a high-pressure, gas scintillation proportional chamber (GSPC), designed for medical imaging in the 30–150 keV energy range, has been investigated through measurement and Monte Carlo simulation. Measurements were conducted on a GSPC containing 4 atm of pure xenon separated from a hexagonal array of seven ultraviolet-sensitive photomultiplier tubes by 1.27-cm-thick fused-silica windows. Experimental measurements of the photopeak efficiency, fluorescence escape efficiency, and the energy collection efficiency were obtained. Results were also obtained for different photon energies and different values of temporal resolution. The measurements were compared with the results obtained from a Monte Carlo simulation designed specifically for investigating the imaging of low-energy photons (below 150 keV) with a gas-filled detector. The simulation was used to estimate photopeak efficiency, fluorescence escape efficiency, photopeak-to-fluorescence escape peak ratio, quantum interaction efficiency, energy collection efficiency, and local energy collection efficiency. The photopeak efficiency of the GSPC relative to that of a 3-in. (7.62-cm)-thick sodium iodide crystal was measured to be 0.284 ± 0.001 at 60 keV and 0.057 ± 0.001 at 140 keV. Of the 60-keV photons incident upon the detector, $70\% \pm 4\%$ interacted in the detector, with $28\% \pm 1\%$ being in the photopeak, as estimated both by experimentation and through the simulation. The maximum energy collection efficiency was found to be 65% at 60 keV, with 46% being deposited within 0.2 cm of the initial photon interaction. The information gained from this study is being used to design an optimized detector for use in specialized nuclear medicine studies.

I. INTRODUCTION

A gas scintillation proportional chamber (GSPC), designed for medical imaging, has been described elsewhere.[1,2] The device, shown in Fig. 1, is designed for imaging radioisotopes with photon energies between 30 and 150 keV. Isotopes of clinical interest in this energy range include thallium-201 (^{201}Tl), tantalum-178 (^{178}Ta), and iridium-191m (^{191m}Ir) (all emit x rays in the 70–75 keV range), which are all used in nuclear cardiology.[3–5] The high intrinsic spatial resolution and energy resolution [4.0-mm full width at half maximum (FWHM) and 5% FWHM at 80 keV, respectively[2,6]] of this device should lead to higher contrast efficiency in this energy range relative to the sodium iodide (NaI), single-crystal scintillation camera. These improved imaging characteristics should also be achievable at high counting rates, since the output pulse is intrinsically Gaussian-shaped and is less than 2 μs and there are minimal space–charge effects within the detector.

The detection of an event in the GSPC follows from a series of processes (summarized in Fig. 2) that occur within the device. The gas volume of the GSPC is divided into two regions: a drift region at low electric field strength (0.05–0.50 kV cm^{-1} atm^{-1}) and a scintillation region (referred to in Fig. 1 as the scintillation gap) at higher electric field strength (1.5–5.0 kV cm^{-1} atm^{-1}).

The photons that escape the patient pass through a collimator and interact in the pressurized xenon (Fig. 2, step 1), primarily by means of the photoelectric effect (97% of the time at 80 keV). The resultant electrons migrate in the drift electric field toward the scintillation region, where the elec-

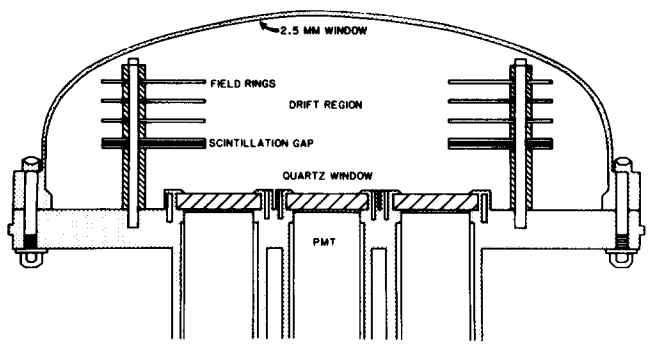

FIG. 1. Gas scintillation proportional chamber. Gamma rays enter the detector through the aluminum window and interact, primarily by the photoelectric effect in the drift region of the detector. The resultant electron swarm drifts toward the scintillation region (or gap). Once in the scintillation region, the electrons attain energy that is high enough to lead to the excitation of the fill-gas atoms. These atoms, upon deexcitation, emit UV, scintillation photons, which are then collected by an array of UV-sensitive PMT's. These tubes are separated from the pressure vessel by fused-silica (i.e., quartz) windows.

 0094-2405/87/010115-09$01.20

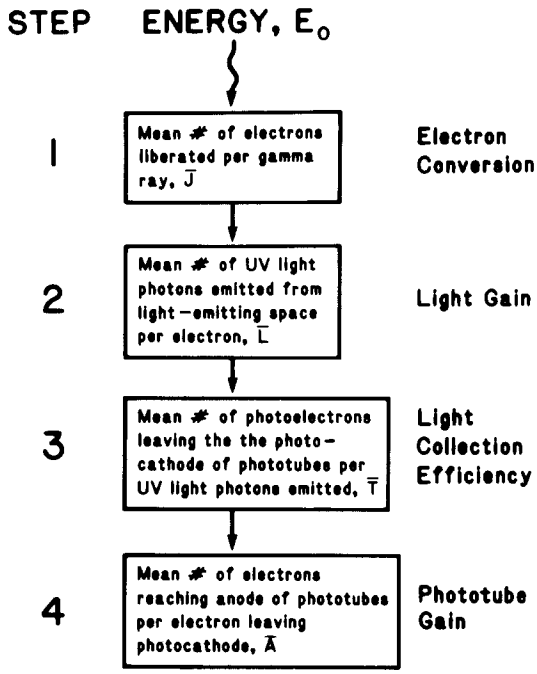

FIG. 2. The secondary scintillation process. (1) The deposition of the photon energy E_0 within the chamber yields J secondary electrons drifting toward the scintillation region. The expected value of J is the electron conversion yield $\bar{J}$. (2) Each of these electrons, as it traverses the scintillation region of the detector, yields the emission of L UV light photons. The mean number of UV photons emitted per electron crossing the scintillation region is the light gain $\bar{L}$. (3) A fraction of these emitted UV photons will be collected by an array of UV-sensitive PMT's. The probability that a UV photon emitted from the scintillation region will yield a photoelectron leaving a photocathode of one of the PMT's is the light collection efficiency $\bar{T}$. (4) For each photoelectron leaving the photocathode of the PMT, a large number of electrons will reach the anode of the PMT. The mean of this number, $\bar{A}$, is referred to as the PMT gain.

tric field is such that the electrons attain sufficient energy between collisions to excite the xenon atoms but not enough to ionize them. Each electron excites many atoms as it drifts across the scintillation region. Upon deexcitation, these xenon atoms emit secondary scintillation photons (Fig. 2, step 2) in the ultraviolet (UV) energy range (mean wavelength of 170 nm for xenon). An array of photomultiplier tubes (PMT's or phototubes) collects the UV photons (Fig. 2, step 3). For each photon collected, $\bar{A}$ electrons, on the average, will reach the anode of the PMT leading to the GSPC signal (Fig. 2, step 4). Anger-camera logic is then used to estimate the location of the event.[7]

During a photoelectric event, the photoelectron is ejected with a kinetic energy equal to that of the incident photon minus the binding energy of the shell from which the photoelectron came. The photoelectron tends to come from the innermost shell that is energetically available to it. For the photon energies above the K edge of xenon (35 keV), the conditional probability that given a photoelectric event which leaves a K shell vacancy, a fluorescent x ray is emitted 0.87 (this value is called the fluorescent yield).[8] If an Auger electron is emitted, it also ionizes and excites a number of atoms, with the resultant electrons drifting toward the scintillation region along with those liberated by the photoelectron. If a fluorescent x ray results, it either is captured within the sensitive volume of the detector or escapes the detector. X rays resulting from K shell vacancies in xenon have energies between 30 and 35 keV, which in 4 atm of xenon have mean free paths of 5 cm.[9]

Detected photoelectric events are separated into two peaks: the photopeak and the fluorescence escape peak. An event occurs in the photopeak if the photoelectric event leads to the emission of an Auger electron, or if a fluorescent x ray is emitted and is detected within a time difference of the detection of the photoelectron that is less than the temporal resolution of the detector (the time necessary to process one event). Events in the photopeak thus represent electron energy liberated in the vicinity of the initial photon interaction (photoelectrons and Auger electrons) and remotely deposited energy (captured fluorescent x rays). Events are counted in the fluorescence escape peak, if the fluorescent x ray (or its resultant photoelectron) escapes the sensitive volume of the detector or if the x ray is detected at a time different from that of detection of the photoelectron by more than the temporal resolution of the detector. In the latter case, the captured fluorescent x ray is counted in a separate x-ray peak. Thus events in the fluorescence escape peak result only from energy deposition from the initial photoelectrons that are locally deposited. Thus if one is to evaluate the imaging capabilities of this device, it is not only important to determine the amount of energy deposited within the detector but also to determine where within the detector this deposition occurred.

Measurements of the photopeak efficiency and the pulse height spectra for a number of radioisotopes with different photon energies can yield much information in this regard. Monte Carlo simulation programs can not only substantiate experimental results but can allow the user to obtain results for various design characteristics without having to rebuild the detector. Some quantities that cannot be readily obtained with experimental data can be defined and estimated by the simulation program. In this report, both experimental data and Monte Carlo simulated data are used to investigate the nature of energy deposition in the GSPC.

Detection efficiency has been investigated for a number of radiation detectors, imaging and nonimaging, both by experimentation and by Monte Carlo simulation. Many of the simulations have been performed for solid detectors (sodium iodide, bismuth germanate, lithium drifted germanium) and at higher energies (0.15–2.0 MeV).[10–12] Many simulations assume that in photoelectric events the entire photon energy is deposited locally, and they do not take into account the emission of the fluorescent x rays.[11,12] This is appropriate in many cases since the probability of fluorescence escape from solid detectors is quite low (the mean free path for iodine fluorescent x rays in sodium iodide is 0.04 cm).[13] This is not an appropriate assumption for gas detectors, since the mean range for xenon x rays in 4 atm of xenon is 5 cm. For these reasons, a Monte Carlo simulation routine, designed specifically for use with gas detectors in the 0–150 keV energy range, has been developed.

II. METHODS

A. Calculation methods

A Monte Carlo program was written in FORTRAN.[20] The detector assumed for the simulation (shown in Fig. 3) was a

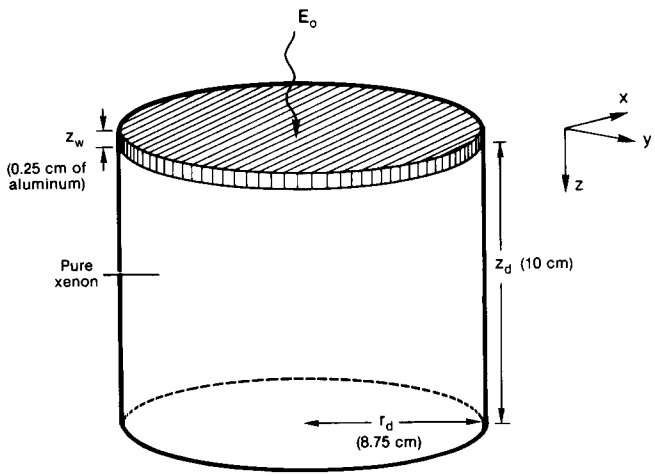

FIG. 3. Assumed detector geometry for the Monte Carlo simulation. The detector was assumed to be a right cylinder of radius r_d and thickness z_d. The photon entrance window of thickness z_w is made of a material assumed to be different from the detector material. The values in parentheses indicate those used in this report.

cylinder of 10-cm height and 8.75-cm radius, which was the geometry of the sensitive volume of the GSPC used to obtain the experimental measurements. The detector was also assumed to have a 0.25-cm aluminum entrance window and to be filled with pure xenon. The photon source was modeled as an ideal pencil beam of gamma rays of energy E_0, normally incident upon the center of the entrance window. The program was designed for low gamma-ray energies (below 150 keV) and thus models the photoelectric effect, the Compton effect, and coherent scattering.[2]

The simulation was started by assuming one of four initial photon interactions [as shown in Fig. 4(a)]: (1) an event which occurs in the entrance window, (2) a photoelectric event in the detector, (3) a Compton scattering event in the detector, and (4) a coherent scattering event in the detector. The simulation was performed for each initial photon interaction for a specified number of histories, and the results of each part were weighted by the probability of the occurrence of that particular initial event and then summed together.

Once the mode of the first interaction was determined, the position within the detector at which this interaction occurred was randomly sampled. One of two subroutines was called, depending upon whether the interaction was a photoelectric event or a scattering event. If the mode of interaction was a photoelectric event, it was determined in which shell the photoelectric effect occurred and whether a fluorescent x ray or an Auger electron was emitted. The subroutine yielded the energy and directional unit vector of the photoelectron, fluorescent x rays, and Auger electrons that were emitted.

The photon scattering angle of the Compton scattered gamma rays was obtained by sampling the Klein–Nishina equation and correcting this distribution by the incoherent scattering factor.[14,15] Once the polar scattering angle was obtained, the scattered photon energy and the energy and scattering angle of the scattered electron were calculated directly. The output of the Compton scattering code was the energies and the directional unit vectors of the scattered photon and electron. The output of the code for coherent scattering was the directional unit vector of the scattered photon.

All of the electrons liberated during a history were assumed to deposit their energy at the point of interaction (with no consideration given to electron range). Photons with energies below 6 keV were also considered to deposit their energy locally. When the processing of the primary photon was completed, the program then followed the secondary photons. Over the span of gas pressures and electron energies considered, the electron ranges are typically less than 1.0 cm (6.7 mm for 110 keV electrons in 4 atm of xenon).[16] The mean free path for 6-keV photons in 1 atm of xenon is less than 3 mm. Although this energy may not be deposited right at the point of interaction, it is deposited within close proximity to this point and therefore these assumptions should not affect the estimates of detection efficiency. The electron ranges associated with the higher energies and the lower pressure (100 keV and 1 atm) may yield some inaccuracies in the local energy deposition efficiency. The mode of interaction and a position of the interaction for the secondary photon (scattered photon or fluorescent x ray) were sampled; if the position was within the detector, the process described above was repeated. It was repeated for each remaining secondary photon until all of the incident photon energy was either deposited within or had exited the detector. This process is illustrated in Fig. 4(b).

Once all the photons associated with a particular history had been followed, it was determined whether all the energy of the incident photon was deposited within the sensitive volume and within the resolving time of the detector. If the electron cloud resulting from a fluorescent x ray that was captured within the detector passed through the scintillation region within a certain time window, its energy was considered to be deposited in the same event as the initial photoelectron. If t_{res} is the resolving time of the detector and t is the time that scintillations from the photoelectron are produced, then $|t - t_{res}|$ is the temporal acceptance window. If the z position of the captured fluorescent x ray was within z_{res} (where z_{res} is the product of the electron drift velocity v_d and t_{res}) of the z position (i.e., depth within the detector) of the initial photoelectron, then the fluorescent x ray electron swarm was considered to be collected within the temporal acceptance window and counted as the same event. If all of the photon energy was collected within the temporal acceptance window, it was counted as a photopeak event. At this point a new history was started and the entire process was repeated.

When the prescribed number of histories had been run, an electron energy deposition spectrum was obtained. This spectrum is a histogram of the number of electrons deposited within the sensitive volume as a function of their energy. A similar spectrum, called the local electron energy deposition spectrum, was obtained for the electrons liberated within 2 mm of the initial x–y position of the pencil beam. These spectra were integrated over energy and normalized by the amount of photon energy incident upon the detector to yield the energy collection efficiency and the local energy collection efficiency, respectively. Thus the energy collection efficiency is the fraction of the incident photon energy that is

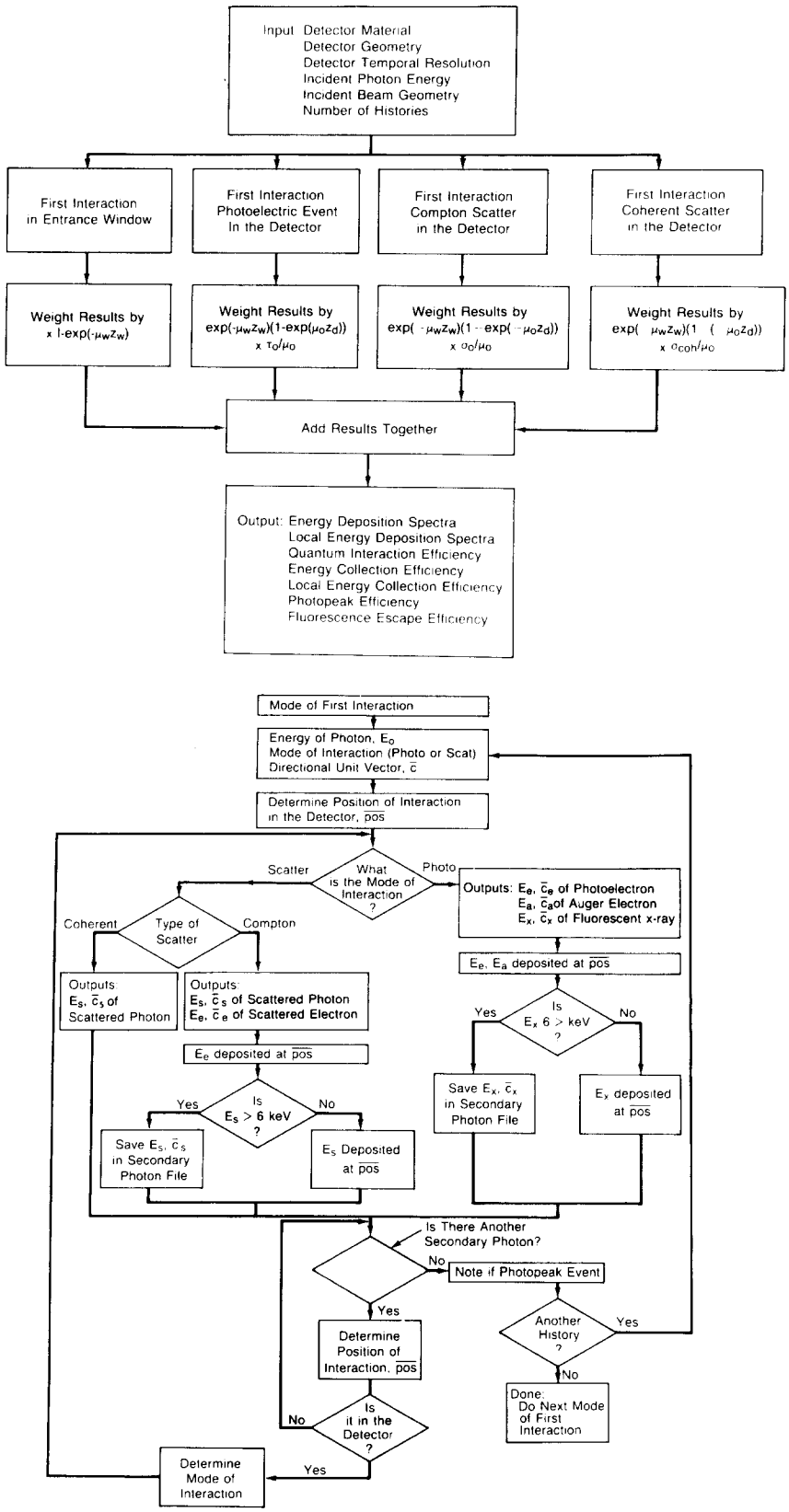

FIG. 4. Block diagram of Monte Carlo simulation. (a) The Monte Carlo simulation program was divided into four parts based upon the mode of the first interaction within the detector. Each was run for a specified number of histories and weighted by the probability of the occurrence of that mode of interaction. These outputs were then summed and the results reported. (b) Within each part, the inputs included the photon energy, mode of first interaction, and the directional unit vector. For the photoelectric effect, the energy deposited by the photoelectron and the Auger electron was determined. For Compton scattering, the energy deposited by the scattered electron was determined. Secondary photons (fluorescent x rays or scattered photons) were then followed, until all of the incident energy either was deposited within or left the detector. The energy deposited and whether it was deposited within 0.2 cm of the incident pencil beam was noted. At this point a new photon history was followed.

deposited within the detector and the local energy collection efficiency is the fraction that is deposited in the immediate vicinity of the incident pencil beam.

The number of photopeak events and the number of escaped fluorescent x rays were normalized by the number of incident photons to yield the photopeak efficiency and the fluorescence escape fraction. The quantum interaction efficiency (QIE) was simply calculated, from the equation

$$\mathrm{QIE} = [1 - \exp(-\mu_0 z_d)]\exp(-\mu_w z_w),$$

where μ_0 is the linear attenuation coefficient for the detector material at E_0 and μ_w is the linear attenuation coefficient for the window material at E_0.

In order to obtain estimates of the uncertainties associated with the various parameters the program was run five times with the same input data, changing only the initial seed to the random number generator. The mean and its standard error were obtained for each of the parameters being calculated from these five independent estimates.

B. Experimental methods

The GSPC contained 4 atm of pure xenon and had a 0.25-cm aluminum entrance window. The drift region was 10 cm thick. The scintillation region was defined by two stainless-steel meshes (0.0025-cm-diam wire, 39.4 wires/cm), separated by 3.1 mm, that were located 5.5 cm above a photomultiplier tube array. The secondary scintillation photons were collected by a hexagonal array of seven UV-sensitive PMT's[21]; these were one center tube and six peripheral tubes. The measurements were obtained with a drift voltage of 2.2 kV across 10 cm (55 V cm^{-1} atm^{-1}) and a voltage of 3.0 kV across the 0.31-cm scintillation region (2.4 kV cm^{-1} atm^{-1}).

The detection efficiency was measured with three different photon sources: americium-241 (^{241}Am, 60-keV gamma ray), xenon-133 (^{133}Xe, 81-keV gamma ray, and x rays between 30 and 35 keV), and technetium-99*m* (^{99m}Tc, 140-keV gamma ray, and x rays between 15 and 20 keV). The radioactive sources were placed at the end of a lead tube, 24 cm long with a 0.4-cm-diam pinhole at the end (2.69×10^{-3} sr solid angle, yielding a beam diameter less than 1.0 cm at the scintillation region).

The signal from the center PMT of the GSPC was filtered by a linear amplifier with 6 μs as the resistive–capacitive (RC) time constants for both integration and differentiation. This signal was input to a multichannel analyzer (MCA)[22] and a pulse height spectrum was obtained. The MCA had an internal single channel analyzer (SCA), and this was used to obtain the number of counts in the photopeak. The acceptance window was set to include the entire peak (typically about 20% of the total energy). The pulses from the SCA were input to a digital scaler and photopeak net counting rates were obtained. This same procedure was also used to measure the photopeak net counting rate for an NaI detector.[23] The photopeak efficiency of the GSPC relative to that of the NaI detector was estimated by taking the ratio of these two values. Utilizing the value calculated from the Monte Carlo simulation for the photopeak efficiency of the NaI detector, the absolute photopeak efficiency for the GSPC was estimated. In order to better resolve the separate peaks and quantify the number of counts in each peak, a Bayesian deconvolution was performed on each spectrum. Bayesian deconvolution is a nonlinear, iterative method that is based upon Bayes theorem.[17–19]

Using the deconvolved ^{133}Xe and ^{99m}Tc spectra, the counts associated with the fluorescence escape peak and the photopeak were determined and used to calculate the photopeak-to-fluorescence escape peak (PP/FE) ratio. This ratio is the number of counts in the photopeak divided by the number of counts in the fluorescence escape peak; it was used, along with the photopeak efficiency, to obtain the fluorescence escape efficiency. This ratio was also measured for ^{133}Xe spectra obtained with various RC time constants on the linear amplifier, in order to determine the effect of temporal resolution on the photopeak efficiency.

The energy collection efficiency is the fraction of the incident photon energy that is deposited within the detector. This was estimated for 60 keV (^{241}Am), 81 keV (^{133}Xe), and 140 keV (^{99m}Tc), using the acquired pulse height spectra and the estimates for the photopeak efficiencies at these energies. The energy deposited within the detector (ED) was the energy integral of the pulse height spectrum. The total energy incident upon the detector was estimated by dividing the product of the number of counts in the photopeak (N) and the energy of the incident photons (E_0) by the measured photopeak efficiency (PPE). The energy collection efficiency (CE) was then the ratio of these two values, i.e.,

$$\mathrm{CE} = \mathrm{ED}^*\mathrm{PPE}/(N^*E_0).$$

The estimate at 81 keV was corrected for the fact that ^{133}Xe also emits a band of cesium x rays between 30 and 35 keV.

III. RESULTS

Figure 5 shows the spectra collected for the three sources used (^{241}Am, ^{133}Xe, and ^{99m}Tc). The ^{241}Am spectrum had a photopeak at 59.5 keV and a peak at 30 keV, which included both xenon x rays that were captured within the detector and the fluorescence escape events. The measured ^{133}Xe spectrum had three peaks: an 81-keV photopeak, a 51-keV fluorescence escape peak, and a 30-keV peak that resulted from fluorescent x rays from the xenon detector and also cesium x rays emitted from the source. The ^{99m}Tc spectrum had a photopeak at 140 keV, an escape peak at 110 keV, and an x-ray peak at 30 keV. It also had a peak at 80 keV due to lead fluorescent x rays from the collimator and a corresponding escape peak at 50 keV. The energy resolution of the GSPC as shown in these spectra is 11.5%, 11.0%, and 8.16% FWHM for 60, 80, and 140 keV, respectively.[1]

The photopeak efficiencies of the GSPC relative to those of the NaI detector are listed in Table I, along with relative photopeak efficiency estimates from the Monte Carlo simulation results. Measurements of the absolute photopeak efficiencies are plotted on Fig. 6, along with estimates of the photopeak efficiencies and fluorescence escape efficiencies obtained from the Monte Carlo simulation for 80 keV at various values of z_{res} (the product of temporal resolution and electron drift velocity). These measured data were con-

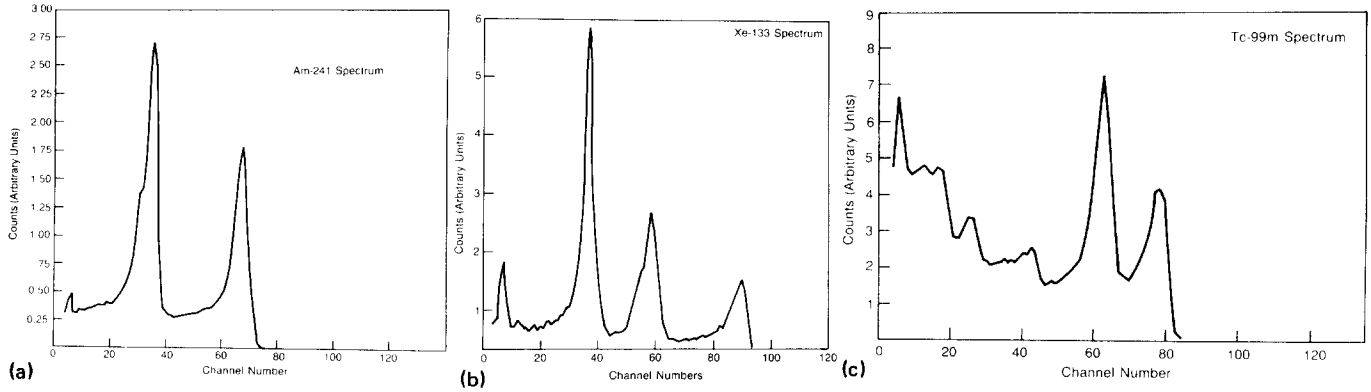

FIG. 5. Pulse height spectra of (a) ^{241}Am, (b) ^{133}Xe, and (c) ^{99m}Tc with the GSPC. The drift voltage was 2.2 kV across 10 cm; the scintillation region voltage was 3.0 kV across 0.31 cm. The PMT signal was filtered with 6 μs of RC shaping; both integration and differentiation. The photopeak, escape peak, and 30-keV x-ray peak are evident in the spectra. For ^{241}Am, the escape peak and the x-ray peak coincide for one peak at 30 keV. For ^{99m}Tc, a lead fluorescent x ray also exists along with its corresponding escape peak (at 80 and 50 keV, respectively).

sistent with a z_{res} value of between 0.1 and 0.2 cm. The probability of interaction in 4 atm of xenon by 60-keV photons is 70%; however, the photopeak efficiency is 28%, because a large fraction of the photoelectric events are present in the fluorescence escape peak. Table II lists the measurements of the fluorescence escape efficiency and the PP/FE ratio for various RC time constants on the shaping amplifier. The fluorescence escape efficiency was dependent upon the resolving time of the detector and its associated electronics.

The estimates of the detection efficiency obtained through the use of the Monte Carlo code for the xenon-filled GSPC described are shown in Figs. 6–9. In these figures, unless otherwise shown, the uncertainty in the simulated data due to random variation yielded a standard deviation whose magnitude was less than the size of the mark used to note the estimate.

The electron energy deposition spectra and the local electron energy deposition spectra for 60, 80, and 140 keV with a fill-gas pressure of 4 atm are illustrated in Fig. 7.

The energy collection efficiency, local energy collection efficiency, and the quantum interaction efficiency are shown in Fig. 8 as a function of photon energy for various fill-gas pressures. The definition of these and all the parameters of efficiency used are as previously defined and as listed in Table III. Figure 8 also shows the fraction of photons that will pass through the aluminum entrance window without interaction. In Fig. 8(b), the estimates of the energy collection efficiency for 4 atm based upon the energy integral of the pulse height spectra and the photopeak efficiencies are shown. The energy collection efficiency for ^{99m}Tc is significantly higher than the estimated value from the Monte Carlo simulation, probably due to the presence of lead x rays from the collimator in the technetium spectrum.

Figure 9 is a plot of collection efficiency, local collection efficiency, and quantum interaction efficiency as a function of fill-gas pressure. Although increasing the fill-gas pressure from 4 to 10 atm increased the efficiency of the detector (by 30% for local collection efficiency, by 26% for collection efficiency, and by 19% for quantum interaction efficiency), further increasing the fill-gas pressure to 18 atm had little effect on the collection and quantum interaction efficiency. The local collection efficiency did increase by an additional 8% when the fill-gas pressure went from 10 to 18 atm.

TABLE I. GSPC photopeak efficiency relative to NaI.[a]

Isotope (energy)	Measured relative photopeak eff.	Simulated relative photopeak eff. z_{res} = 2 mm	Simulated relative photopeak eff. z_{res} = 1 mm
^{241}Am (59.5 keV)	0.284 ± 0.001	0.278 ± 0.010	0.230 ± 0.001
^{133}Xe (81 keV)	0.152 ± 0.001	0.199 ± 0.007	0.170 ± 0.009
^{99m}Tc (140 keV)	0.057 ± 0.001	0.052 ± 0.002	0.045 ± 0.002

[a] GSPC photopeak efficiency values were normalized by the values for NaI. These values are compared to results from the Monte Carlo simulations for two different values of z_{res}. The measured values were consistent with the simulated results for a z_{res} value of between 0.1 and 0.2 cm.

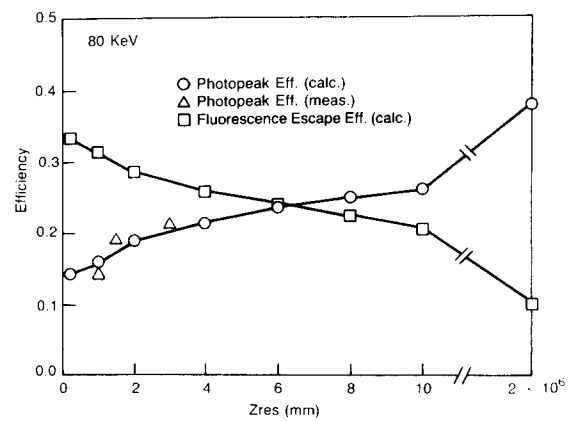

FIG. 6. Photopeak efficiency of GSPC vs z_{res}. The product of v_d and t_{res} equals z_{res}, where v_d is the drift velocity of the electrons in the drift region of the GSPC, and t_{res} is the device's resolving time. If the position of the captured fluorescent x ray has a z coordinate that is within z_{res} of the z coordinate of the position of the initial photoelectric event, then the two are counted as a single energy deposition. Changing z_{res} affects the photopeak efficiency of the GSPC by shifting events from the photopeak to the fluorescence escape peak. The open circles represent data obtained from the Monte Carlo simulation; the triangles represent measured data.

TABLE II. Photopeak-to-fluorescence escape ratio and the fluorescence escape efficiency for various time constants.

RC time constant	PP/FE ratio	Fluor. escape efficiency
4 μs	0.686 ± 0.010	0.222 ± 0.003
6 μs	0.802 ± 0.010	0.190 ± 0.003
12 μs	1.006 ± 0.010	0.149 ± 0.002

IV. DISCUSSION

The measured and calculated values for photopeak efficiency, fluorescence escape efficiency, and energy collection efficiency were in very good agreement. The changes in these parameters when photon energy, temporal resolution, and pressure were varied were well predicted by the model. The model was then used to predict parameters that could not be measured.

The quantum efficiency of the GSPC was high in the energy range between 40 and 100 keV with a maximum at 60 keV of 0.83 for 10 atm. In this energy range, the GSPC's potential for high resolution will best be realized, since at higher energies the loss of system spatial resolution is generally caused by factors other than low intrinsic resolution due to insufficient numbers of collected quanta. The quantum efficiency is somewhat lower for energies above 100 keV.

Utilizing the plots of the various parameters of detection efficiency as a function of energy, an optimum energy with regard to efficiency can be defined. This optimum energy is a function of the product of the gas pressure and the detector thickness, increasing as this product increases. Conversely, for a particular photon energy, it is possible to define a detector with a particular thickness and gas pressure that yields maximal detection efficiency at that energy. For example, if the device is to image the x rays from ^{201}Tl, ^{178}Ta, and ^{199m}Ir, an optimum detector configuration can be defined.

The local electron spectrum included the photoelectron and the Auger electrons that deposit their energy in the vicinity of the incident photon beam. However, a significant

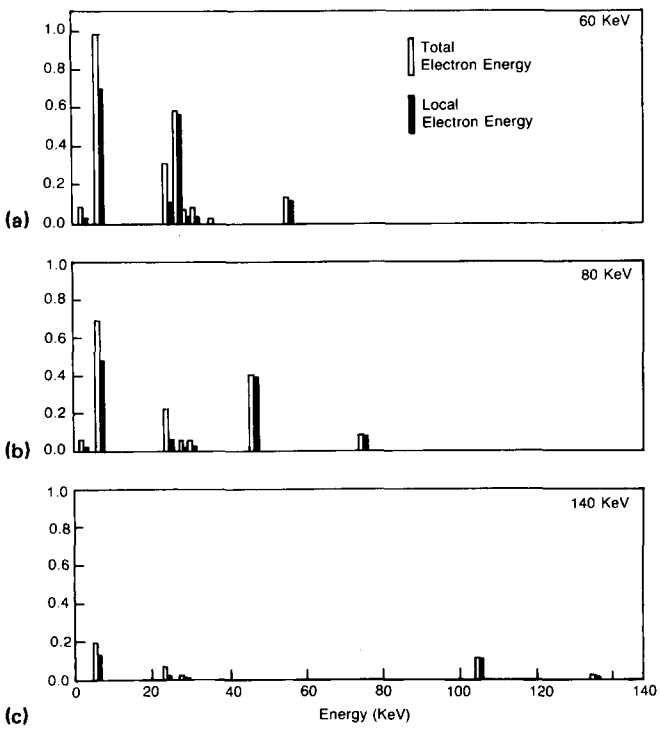

FIG. 7. Electron energy deposition spectra. The total electron energy deposition spectra and the local electron energy deposition spectra are shown for (a) 60, (b) 80, and (c) 140 keV. The detector is cylindrical with 4 atm of pure xenon; its radius is 8.75 cm and its depth 10 cm. The local electron energy deposition spectra are histograms of the electron energy that is deposited within 0.2 cm of the incident pencil beam of incident photons. The total electron energy deposition spectra are histograms of the electron energy that is deposited within the whole detector. These data are the results of a Monte Carlo simulation of the GSPC.

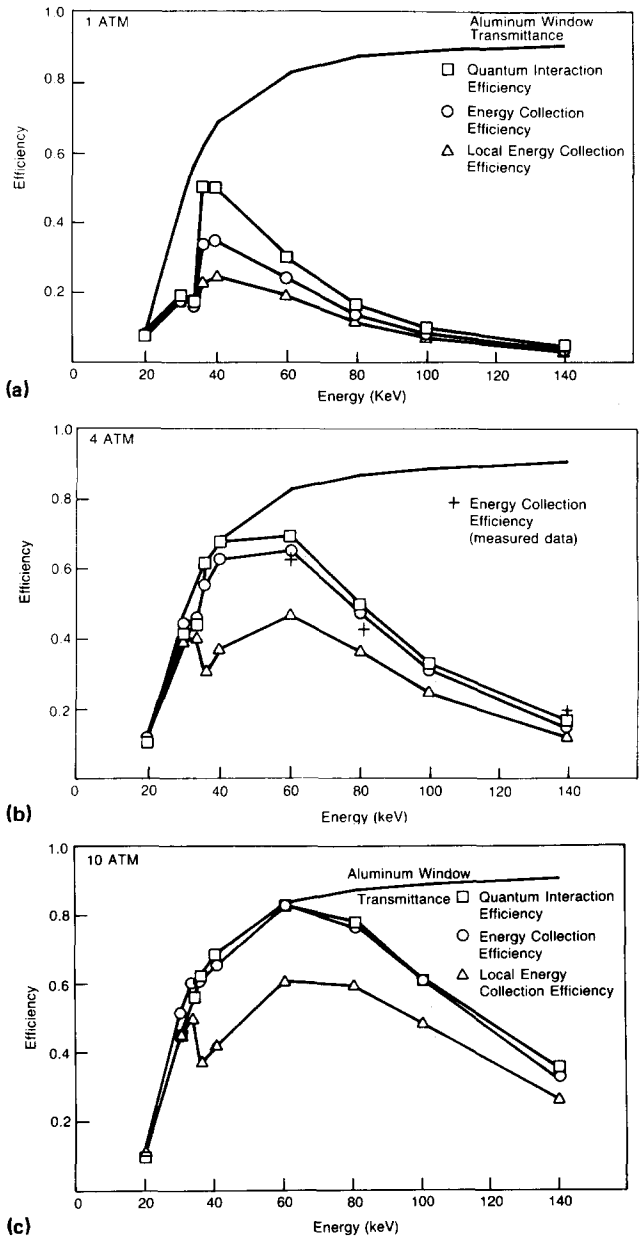

FIG. 8. Detection efficiency of the GSPC and NaI detector. The transmittance of the 0.25-cm aluminum window, the quantum interaction efficiency, the total energy collection efficiency, and the local energy collection efficiency of the GSPC are shown for fill-gas pressures of (a) 1, (b) 4, and (c) 10 atm. These data are the results of a Monte Carlo simulation of the GSPC. In part (b), measured data of the energy collection efficiency at 60, 81, and 140 keV are shown.

TABLE III. Definition of various efficiency parameters.

Photopeak efficiency (PPE)	Fraction of incident photons leading to the deposition of all the photon energy in the detector within the temporal resolution of the detector.
Quantum interaction efficiency (QIE)	Probability of an incident photon having an interaction in the detector.
Energy collection efficiency	Fraction of the incident photon energy that is deposited within the detector.
Local energy collection efficiency	Fraction of the incident photon energy that is deposited within 2 mm of the incident, photon, pencil beam.
Fluorescence escape efficiency	Fraction of the incident photons that lead to a fluorescent x ray either escaping the detector or being captured but being counted as a separate event from the photoelectron.
Photopeak-to-fluorescence escape (PP/FE) ratio	Ratio of the events in the photopeak to those in the fluorescence escape peak.

fraction of the energy deposited within the detector was due to the capture of fluorescent x rays and was not located near the point of the initial gamma-ray interaction. This fraction of the deposited energy does not lead to accurate spatial information, and would be deemed less useful in an imaging device. This was demonstrated in Fig. 8, where the local energy collection efficiency is substantially less than the total energy collection efficiency. Although in a 4-atm chamber, 65% of the photon energy incident upon the GSPC in the form of 60-keV photons are deposited within the detector, 46% of the incident photon energy is deposited near the point of the initial interaction, leading to useful spatial information. The quantum interaction efficiency estimates indicated that for incident 60-keV photons in a 4-atm chamber, 70% of the photons interacted within the detector. Figure 8 illustrates that a large fraction of these photons that interact lead to captured fluorescent x rays that can compromise the imaging capability of the detector.

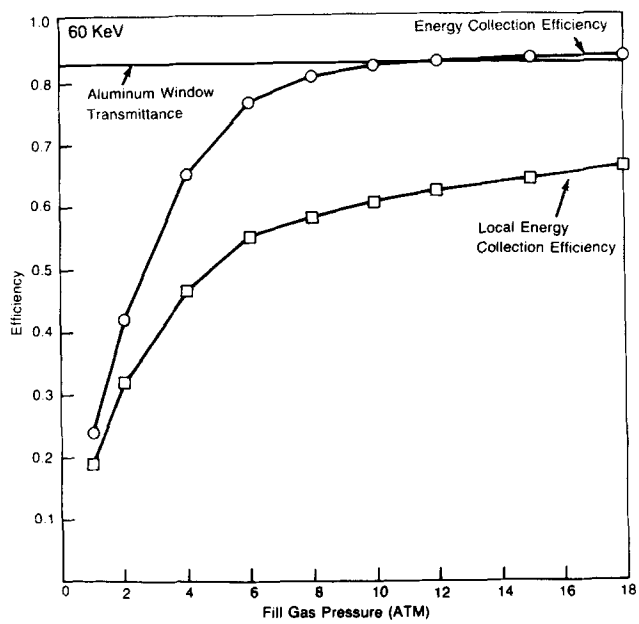

FIG. 9. GSPC detection efficiency vs fill-gas pressure. The energy collection efficiency, the local energy collection efficiency, and the fluorescence energy escape fraction are plotted as a function of fill-gas pressure. The detector is a cylinder of pure xenon with a radius of 8.75 cm and a depth of 10 cm. These data are for 60-keV incident photons. The transmittance of the aluminum window is also shown. These data are the result of the Monte Carlo simulation.

The photopeak efficiency is substantially lower than the quantum detection efficiency. Table I also indicates that the photopeak efficiencies for the GSPC varied greatly from the values for an NaI detector even at 60 keV, where the values might be expected to be similar. The photoelectric events in the GSPC tended to be accumulated in two peaks rather than in one as in the NaI detector. In the NaI detector, almost all of the fluorescent x rays interact in the vicinity of the initial event, and all of these lead to light photons being collected along with those from the initial photoelectron within the temporal resolution of the detector. Due to the long range of fluorescent x rays in the GSPC and the long drift times of the electrons (it takes about 50–100 μs for electrons to drift from the top of the drift region to the scintillation region of the detector), many photoelectric events, even if the fluorescent x ray is captured, will be counted in the fluorescence escape peak. The fluorescence escape peak thus contains many events, all of which yield good spatial information. Increasing the resolving time to include fluorescence capture events in the photopeak leads to poorer spatial information. The comparison between the electron energy deposition spectra and the local electron energy deposition spectra (Fig. 7) demonstrates the effect of fluorescence capture within the gas-filled detector.

It is often preferable to have the shortest possible temporal resolution, e.g., when performing first-pass cardiac studies, where the detector must collect as much data as possible in a short time.[5] As seen in Table II, reducing the temporal resolution of the detector shifts events from the photopeak to the escape peak. Even for extremely short resolving times, there will still be a substantial photopeak. An Auger electron is sometimes emitted instead of a fluorescent x ray following a photoelectric event, thus leading to photopeak events. In such cases, however, much more information resides in the fluorescence escape peak than in the photopeak. Efficient use of the data available from the GSPC may require counting both peaks.

ACKNOWLEDGMENTS

The authors would like to thank Jane Gilmore and David Klemm for their excellent art work and Dorothy Sawicki for her invaluable help in editing this manuscript. This research was funded by USPHS Grant No. R01 HL24496.

[1]F. H. Fahey, R. E. Zimmerman, P. F. Judy, and R. C. Lanza, Med. Phys. **13**, 25 (1986).
[2]F. H. Fahey, D.Sc. thesis (Harvard University, 1986).
[3]H. W. Strauss, K. Harrison, J. K. Langan, E. Lebowitz, and B. Pitt, Circulation **51**, 641 (1975).

[4]B. L. Holman, R. E. Zimmerman, L. V. Bifolk, and R. D. Neirinckx, J. Nucl. Med. **20**, 538 (1979).
[5]S. Treves, C. Cheng, A. Samuel, R. Lambrecht, B. Babchyck, R. Zimmerman, and W. Norwood, J. Nucl. Med. **21**, 1151 (1980).
[6]F. H. Fahey, R. E. Zimmerman, and R. C. Lanza, J. Nucl. Med. **26**, 43 (1985).
[7]R. L. Richardson, in *Nuclear Medicine Physics, Instrumentation, and Agents*, edited by F. D. Rollo (Mosby, St. Louis, 1977), pp. 231–270.
[8]R. W. Fink, R. C. Jopson, H. Mark, and C. D. Swift, Rev. Mod. Phys. **38**, 513 (1966).
[9]W. H. McMaster, N. K. Del Grande, J. H. Mallett, and J. H. Hubbell, *Compilation of X-ray Cross Sections, UCRL-50174* (U.S. Department of Commerce, Washington, DC, 1969).
[10]M. J. Berger and S. M. Seltzer, Nucl. Instrum. Methods **104**, 317 (1972).
[11]J. J. Steyn, R. Huang, and D. W. Harris, Nucl. Instrum. Methods **107**, 465 (1973).
[12]M. Capponi, J. Massa, M. Piccinini, and M. Poli, Nucl. Instrum. Methods **217**, 465 (1983).
[13]*Radiological Health Handbook* (U.S. Department of Health, Education, and Welfare, Rockville, MD, 1970), p. 137.
[14]R. D. Evans, *The Atomic Nucleus* (McGraw–Hill, New York, 1955), p. 682.
[15]J. H. Hubbell, W. J. Viegele, E. A. Briggs, R. T. Brown, D. T. Cromer, and R. J. Howerton, J. Phys. Chem. Ref. Data **4**, 471 (1975).
[16]L. Katz and A. Penfold, Rev. Mod. Phys. **24**, 28 (1952).
[17]T. J. Kennett, W. V. Prestovich, and A. Robertson, Nucl. Instrum. Methods **151**, 285 (1978).
[18]T. J. Kennett, W. V. Prestovich, and A. Robertson, Nucl. Instrum. Methods **151**, 293 (1978).
[19]T. J. Kennett, P. M. Brewster, W. V. Prestovich, and A. Robertson, Nucl. Instrum. Methods **153**, 125 (1978).
[20]FORTRAN 77 run on a VAX 11/780.
[21]Hammamatsu, Model R208.
[22]Northern Scientific, Model NS-900.
[23]3-in.-diam ×3-in.-length NaI detector, manufactured by Bicron.